

Nanoparticle Scattering for Multijunction Solar Cells: The Tradeoff Between Absorption Enhancement and Transmission Loss

Alexander Mellor, Nicholas P. Hylton, Hubert Hauser, Tomos Thomas, Kan-Hua Lee, Yahya Al-Saleh, Vincenzo Giannini, Avi Braun, Josine Loo, Dries Vercruyse, Pol Van Dorpe, Benedikt Bläsi, Stefan A. Maier, and N. J. Ekins-Daukes

Abstract—This paper contains a combined experimental and simulation study of the effect of Al and AlInP nanoparticles on the performance of multijunction (MJ) solar cells. In particular, we investigate oblique photon scattering by the nanoparticle arrays as a means of improving thinned subcells or those with low diffusion lengths, either inherently or due to radiation damage. Experimental results show the feasibility of integrating nanoparticle arrays into the antireflection coatings of commercial InGaP/InGaAs/Ge solar cells, and computational results show that nanoparticle arrays can improve the internal quantum efficiency via optical path length enhancement. However, a design that improves the external quantum efficiency of a state-of-the-art cell has not been found, despite the large parameter space studied. We show a clear trade-off between oblique scattering and transmission loss and present design principles and insights into how improvements can be made.

Index Terms—Light trapping, multijunction (MJ) solar cell, nanophotonics, radiation hardness.

Manuscript received January 13, 2016; revised July 14, 2016; accepted August 12, 2016. Date of publication September 9, 2016; date of current version October 19, 2016. This work was supported by the European Space Agency (4000110969/14/NL/FE), the European Commission (FP7-248154 and H2020-DLV-657359), the Leverhulme Trust, and the Royal Society. The fabrication and characterization of Sample Set 2 and the computational investigation were funded by the European Space Agency under Contract 4000110969/14/NL/FE. The fabrication and characterization of Sample Set 1 were funded by the European Commission under the FP7 project “Plasmon Resonance for Improving the Absorption of solar cells (PRIMA)” Project 248154. Radiation tests were performed at Delft University of Technology and funded by AZUR SPACE. The work of A. Mellor was supported by the European Commission through a Marie Skłodowska Curie International Fellowship. The work of N. J. Ekins-Daukes was supported by the Royal Society through an Industry Fellowship.

A. Mellor, N. P. Hylton, K.-H. Lee, Y. Al-Saleh, V. Giannini, A. Braun, S. A. Maier, and N. J. Ekins-Daukes are with the Department of Physics, Imperial College London, London SW7 2AZ, U.K. (e-mail: a.mellor@imperial.ac.uk; n.hylton@imperial.ac.uk; kanhwa@gmail.com; yahya.al-saleh09@imperial.ac.uk; v.giannini@imperial.ac.uk; a.braun@imperial.ac.uk; s.maier@imperial.ac.uk; n.ekins-daukes@imperial.ac.uk).

H. Hauser and B. Bläsi are with the Fraunhofer Institute for Solar Energy Systems ISE, 79110 Freiburg Germany (e-mail: hubert.hauser@ise.fraunhofer.de; benedict.bläsi@ise.fraunhofer.de).

T. Thomas is with Imperial College London, London SW7 2AZ, U.K. (e-mail: tomos.thomas08@imperial.ac.uk).

J. Loo and D. Vercruyse are with IMEC, 3001 Leuven, Belgium (e-mail: josine.loo@imec.be; dries.vercruyse@imec.be).

P. Van Dorpe is with IMEC, Leuven 3001, Belgium, and also with the Department of Physics and Astronomy, Katholieke Universiteit Leuven, 3000 Leuven, Belgium (e-mail: pol.vandorp@imec.be).

Color versions of one or more of the figures in this paper are available online at <http://ieeexplore.ieee.org>.

Digital Object Identifier 10.1109/JPHOTOV.2016.2601944

I. INTRODUCTION

We evaluate the use of aluminum nanoparticle (NP) arrays as a means of improving the performance of high-efficiency multijunction (MJ) solar cells. NP arrays have the potential to increase the absorption in solar cells by scattering incident photons into oblique modes within the absorber layers with increased path lengths. This allows thinner layers to be used, which can improve the performance of many types of MJ solar cells, as well as reducing costs. The use of both NP arrays and surface textures for absorption enhancement has been studied extensively in various types of thin-film solar cells [1]–[3], as well as in bulk c-Si solar cells [4]–[7]. NP arrays have also shown promising results in optically thin III–V single-junction solar cells [8], [9]. This provides motivation for investigating their use in III–V MJ solar cells: the highest efficiency PV technology that exists today.

In MJ solar cells, the main applicability of oblique photon scattering is for subcells, in which the minority carrier diffusion length is shorter than the thickness that is normally required for full absorption. There are many examples of this in present technologies. In space, solar cells are subject to high-energy electron and proton irradiation, reducing diffusion lengths and photocurrent; this is most pronounced in the $In_{0.01}GaAs$ middle cell [10], [11]. On Earth, many high-efficiency concentrator solar cells rely on materials such as GaInNAs [12] and $In_0.3Ga_0.7As$ [13] with low diffusion lengths, either due to intrinsic material quality or lattice mismatching with adjacent subcells. Similarly, in III–V-on-Si MJ tandems, lattice mismatching leads to high defect densities and low diffusion lengths in the III–V top cell [14]–[16]. All these technologies would be improved if one or more of the subcells could be thinned while maintaining strong photon absorption.

In these examples, the subcell to be enhanced is not the bottom cell but, rather, one of the upper cells. The NP array must, therefore, be placed on the front of the device and not on the rear, since photons intended for one of the upper subcells will not reach the rear, being strongly absorbed in the bottom cell. This has the added complication that the NP array must not only achieve strong oblique scattering but must maintain an overall broadband transmission that is close to a state-of-the-art double-layer antireflection coating (ARC) as well.

Aluminum NP arrays have the potential for strong scattering but low transmission loss and have led to a 22% integrated

efficiency enhancement in electrically thinned GaAs photodiodes without ARCs [8]. A more recent computational study has shown that Al NP arrays embedded in a single-layer ARC exhibit transmission losses compared with a double-layer ARC, but that these losses can be very small [17]. Motivated by these results, we investigate cylindrically shaped Al NPs embedded in a double-layer ARC. We focus particularly on the tradeoff between absorption enhancement via oblique scattering on one hand and transmission loss due to increased reflection and parasitic absorption on the other.

In this work, state-of-the-art InGaP/InGaAs/Ge space solar cells were fabricated with Al NP arrays embedded in the double-layer ARC. The solar cells were subjected to irradiation tests. This reduces the minority carrier diffusion lengths so that charge carriers are not efficiently collected from the whole subcell, but rather a thinner region close to the junction. This way, the effect of NP scattering on current generation in electrically thinned subcells is investigated. In parallel, a fast electrooptical simulation technique was developed and validated against the experimental data. Section II describes the fabricated prototypes, irradiation conditions, and the characterization and simulation methods used. Section III presents quantum efficiency measurements before and after irradiation, as well as simulations of the experimental samples. In Section IV, the simulation technique is used to survey a large design space encompassing NP diameter, height, array period, and positioning in the ARC. Here, both metallic Al and semiconductor AlInP NPs are investigated. A clear tradeoff between oblique scattering and transmission loss is shown, the possibilities and limitations of this technology are discussed, and design principles are established. There is general discussion of results in Section V, and Section VI concludes this paper.

II. METHODS

A. Prototype Fabrication

Periodic arrays of cylindrical Al NPs were integrated into the ARC of state-of-the-art triple-junction solar cells. The shape and material were chosen based on [8] and [18], respectively. Two different sample sets were produced using two different nanofabrication techniques: e-beam lithography and nanoimprint lithography. In both cases, the underlying devices were triple-junction GaInP/In_{0.01}GaAs/Ge space solar cells produced at Azur Space Solar Power GmbH. The epi structure is marginally different for each sample set, although no specific details are given.

Sample Set 1: Custom triple-junction solar cells with double-layer AlO_x/TiO_x ARCs were produced at AzurSpace. Al NP arrays were realized on top of the ARC over 300 × 300 μm² areas by e-beam lithography. Different arrays were produced with periods of 200, 300, and 400 nm. In each case, the NPs had a diameter of 80 nm and a height of 30 nm. The top part of Fig. 1 shows scanning electron microscopy (SEM) images of the 300-nm period NP array, as well as schematic of the position of the NPs in the ARC. The NPs have smooth rounded edges.

Sample Set 2: Commercial triple-junction 3G30 space solar cells were produced at AzurSpace GmbH with full

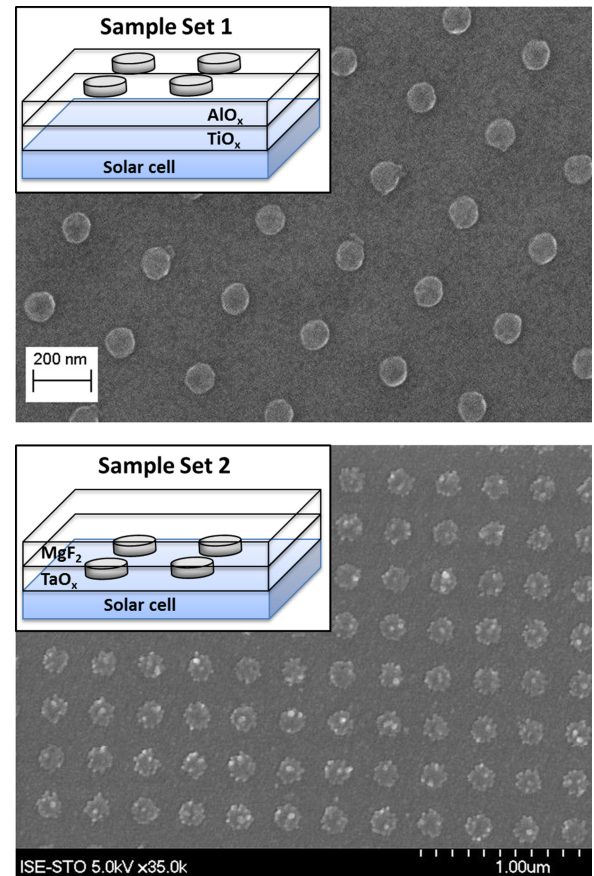


Fig. 1. SEM images of the deposited NP arrays. (Insets) Schematics of the position of the NP arrays in the ARC in the two experimental samples. (Top) Sample Set 1. (Bottom) Sample Set 2. For Sample Set 1, the SEM image shows the 300-nm period array. Similar results were achieved for the 200- and 400-nm period arrays. The SEM images have different scales.

metallization but no ARC. Double-layer MgF₂/TaO_x ARCs with Al NP arrays embedded within the TaO_x layer were then fabricated. The NP arrays were realized over the whole solar cell area by nanoimprint lithography [19]. The mastering was done using interference lithography as described in [20]. Details of the complete nanofabrication process chain including the liftoff process can be found in [21]. The NPs had an array period of 300 nm, a diameter of 150 nm, and a height of 15 nm. The NPs were separated from the semiconductor by a 15-nm-thick TaO_x spacer layer. The bottom part of Fig. 1 shows an SEM image of an NP array and a schematic of the position of the NPs in the ARC. The NPs are circular in shape but with rough edges. We attribute this to the porosity of the thin Al film, from which the NPs were realized.

The use of different ARC-material combinations in the two sample sets is solely due to ease of fabrication, given that ARC deposited took place in different laboratories for sets 1 and 2.

B. Characterization Methods and Irradiation Testing

External quantum efficiency (EQE) and reflectance spectra were measured using a combination of xenon and halogen lamps coupled to a Bentham Instruments monochromator. The

monochromatic light was then delivered via a 600- μm core optical fiber to a custom-built microscope system, which illuminated a small ($150 \times 150 \mu\text{m}^2$) area. EQE measurements were made under voltage bias and light bias using three LEDs for the spectral regions corresponding to each subcell. The EQEs were calibrated by measuring the incident spectrum using a calibrated Si detector. For the reflectance measurement, the reflected light was measured using calibrated Si and Ge detectors and the device reflectance extracted from the raw data using corresponding measurements of a reference mirror.

Sample Set 2 was also subject to irradiation testing. The cells were irradiated with a $1 \times 10^{15} \text{ cm}^{-2}$ fluence of 1-MeV electrons, a typical value for geostationary missions. This was followed by photon annealing under AM0 at 25 °C for 60 h, then dark annealing at 60 °C for 24 h. This is in accordance with the standard of the European Cooperation for Space Standardization [22]. The samples were measured before and after irradiation testing; these results are denoted beginning of life (BOL) and end of life (EOL), respectively.

C. Simulation Technique

An electrooptical simulation tool has been developed to model MJ solar cells with NP arrays embedded somewhere in the ARC. The method is based on coupling an optical rigorous coupled wave analysis model to a 1-D electrical drift-diffusion model. The former is implemented using commercial package GdCalc [23] and the latter is semianalytical [24]. This combined model is a simplification of that in [25] and [26]. The calculation yields the expected EQE of the simulated device. In addition to the EQE, the simulation also calculates the diffraction efficiencies with which incident light is coupled to photonic modes within the solar cells. The simulation runs on a standard desktop computer and can calculate the spectral response of a given nanostructured devices in a few minutes, allowing thousands of designs to be evaluated in a day. The optical part of the model is subject to convergence testing to ensure numerical accuracy.

It is known that Al NPs deposited via evaporation contain both oxide contamination in their bulk, as well as a shell of oxide on the surface. To simulate this, following [27], the Al NPs are taken to consist of 80% Al and 20% Al_2O_3 , and the optical constants are calculated using a Bruggeman effective medium theory with Al and Al_2O_3 data taken from [28] as input. A core-shell geometry has not been used for ease of simulation. For Sample Set 2, we consider an additional 20% air content given the porosity that is evident in the bottom part of Fig. 1. Optical constants for the other materials and the electrical parameters of the MJ solar cells were measured in-house by our collaborators. The effect of irradiation is accounted for in the electrical part of the model via the minority carrier diffusion lengths in the InGaP and InGaAs subcells.

III. COMBINED EXPERIMENTAL AND SIMULATION STUDY

A. Experimental Results

The solid curves in Fig. 2 show the measured top- and middle-cell EQEs for Sample Set 1, demonstrating the losses induced

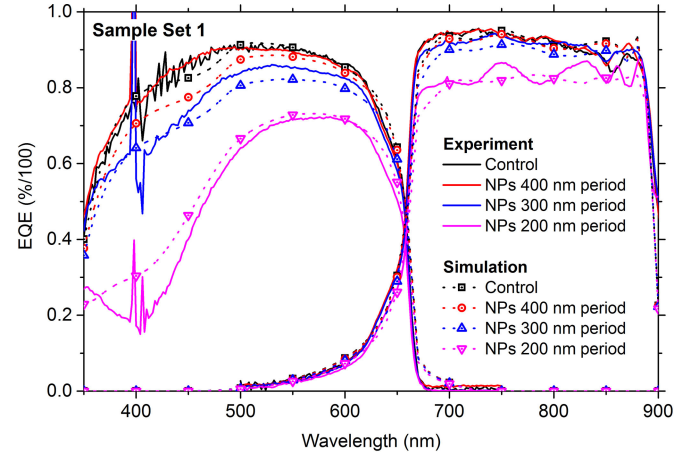


Fig. 2. Measured and simulated EQE for Sample Set 1. The NPs have a diameter of 80 nm and a height of 50 nm. The array periods are shown in the legend.

by NP arrays of different dimensions. The sparse 400-nm array shows no loss compared with the control, whereas increasing losses are observed for the denser 300- and 200-nm-period arrays. The greatest loss is in the top-cell EQE due to the localized plasmon resonance [29] at around 400 nm. This could be mitigated by realizing smaller NPs, which resonate in the ultraviolet [8], [30], [31]. Sample Set 1 has optically thick layers (i.e., each subcell absorbs close to 100% of incident photons in its respective spectral range). Therefore, the experimental EQE is not informative about the positive effect of oblique scattering. However, this is investigated in Section III-B using the simulation results. The very sharp feature at 400 nm is a measurement artefact caused by the switching of the xenon and halogen source lamps in the EQE apparatus.

The solid curves in Fig. 3 show the measured top- and middle-cell EQEs for Sample Set 2. Since these samples were irradiated, results are shown both at BOL [see Fig. 3(a)] and EOL [see Fig. 3(b)]. Here, the NPs lead to a broadband loss of 10% and 20% absolute in the top and middle cells, respectively. This is observed both at BOL and EOL.

The top-cell EQE of the control at BOL is lower than would be expected for this type of solar cell. We believe this is due to a degradation of the front-surface passivation in this sample set. The epitaxy and ARC deposition were performed by different organizations in this experiment, which is the likely cause of this degradation. We were able to fit the top-cell EQE with the same front-surface recombination velocity for both control and NP solar cells, suggesting that the level of degradation is the same for both. We, therefore, do not believe that this affects the experiment.

Table I shows the fraction of the integrated EQE that remains at EOL for both subcells. At EOL, the minority carrier diffusion lengths are degraded in both top and middle cells so that charge carriers are not efficiently collected from the whole subcell, but rather a thinner region close to the junction. Hence, the EQE of the NP solar cell at EOL gives experimental insight into any positive effect of NP scattering in an electrically thinned subcell.

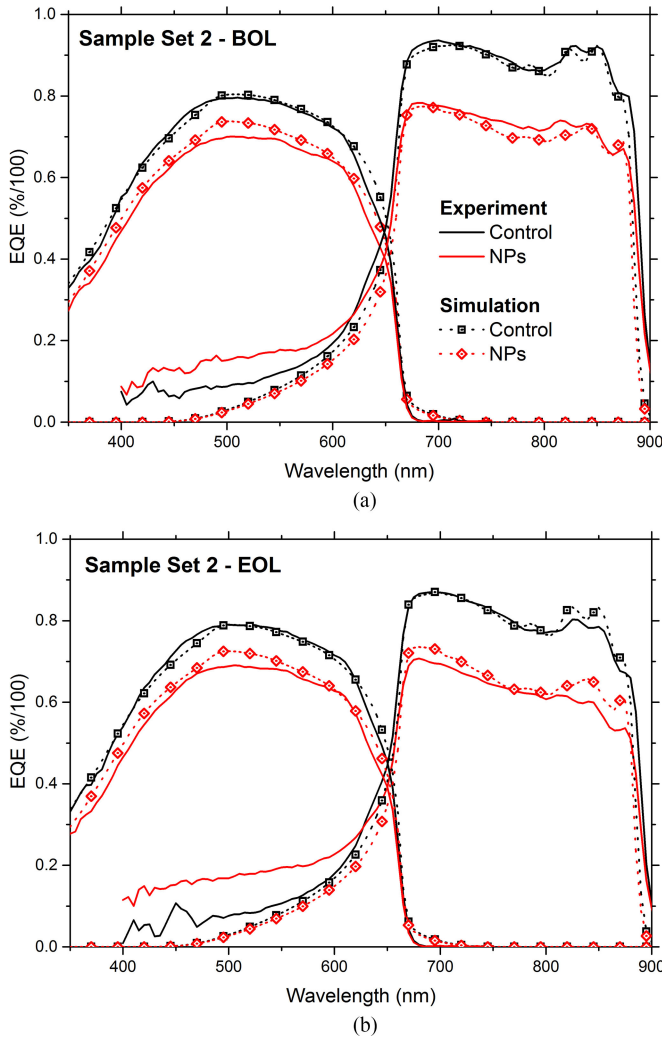


Fig. 3. Measured and simulated EQE for Sample Set 2. The NPs have a diameter of 150 nm, a height of 15 nm, and an array period of 300 nm. (a) Before irradiation exposure (BOL). (b) After irradiation exposure (EOL).

TABLE I
FRACTION REMAINING OF INTEGRATED EQE AT EOL

	Top Cell / %	Middle Cell / %
Control	99	90
NPs	99	90

The fact that the fraction remaining is the same for the control and NP samples suggests that there is negligible positive effect due to oblique scattering in the NP device.

B. Simulation of Experimental Samples

Figs. 2 and 3 also show the results of electrooptical simulations of the experimental samples, demonstrating a good agreement between experiment and simulation. Using the simulation, we are able to probe the oblique photon scattering inside the solar cell. Since the NP array is periodic, incident photons can only be coupled into the semiconductor bulk via a finite set of

propagating diffraction orders, whose polar angles are determined by the array period [32]. The top row of Fig. 4 shows the polar angles of these orders for each NP solar cell fabricated in this study. The bottom row shows the total transmission into the solar cell, as well as the diffraction efficiencies, i.e., the fraction of incident photons coupled into each set of transmitted orders. (Different diffraction orders with the same polar angle are grouped together.)

For each solar cell in Sample Set 1, nearly 100% of transmitted photons are coupled into the undeflected zero order, with a depreciable fraction being coupled into oblique orders. In Sample Set 2, there is an appreciable coupling of incident photons into oblique orders, with around 15–20% being coupled into the first set and 0–5 % being coupled into the second set. However, this level of scattering is clearly not sufficient to improve the performance of an electrically thinned subcell, as is evidenced by the experimental results in Table I.

The fact that oblique scattering into the semiconductor is possible for Sample Set 2 but not for Sample Set 1 is due to the position of the NPs in the ARC. This is discussed in detail in Section IV-B2.

C. Summary of Combined Experimental and Simulation Study

It has been shown that integration of NPs into the ARC can lead to minimal transmission losses in some cases (Sample Set 1, 400-nm period) and appreciable oblique scattering in others (Sample Set 2). However, both phenomena have not been observed in the same solar cell, and in no case has the level of oblique photon scattering been seen to have a significant effect on the EQE of a subcell that has been electrically thinned by irradiation. To determine if this limitation is particular to the fabricated NP arrays, or endemic to aluminum nanodisks integrated into the ARC, a much wider design space is studied computationally in the following section.

IV. WIDER SIMULATION STUDY

The electrooptical simulation has been used to study a range of NP-array dimensions and positions in the ARC. Simulations were made for the three configurations, shown in Fig. 5, these being the NPs embedded in the ARC bottom layer (Configuration 1), embedded in the ARC top layer (Configuration 2), and sitting on top of the ARC (Configuration 3). For each configuration, simulations have been made over a range of array periods Λ , NP diameters D , and NP heights H . Nearly 6000 spectra were calculated, taking in every permutation of the 3-D parameter space encompassing the ranges $200 < \Lambda < 400$ nm, $20 < r < 190$ nm, and $10 < h < 50$ nm, with a 10-nm step size in each case. A planar benchmark structure was also simulated, which has an identical ARC but no NPs. In all cases, the ARC is $\text{AlO}_x/\text{TiO}_x$.

In all simulations, the AlO_x and TiO_x layer thickness are taken to be 60 and 60 nm, respectively. These values were chosen by considering a solar cell equivalent to the planar control in Sample Set 1, and computationally optimizing the net photocurrent, i.e., that produced by the limiting subcell. Since the Ge subcell produces excess photocurrent in this type of solar

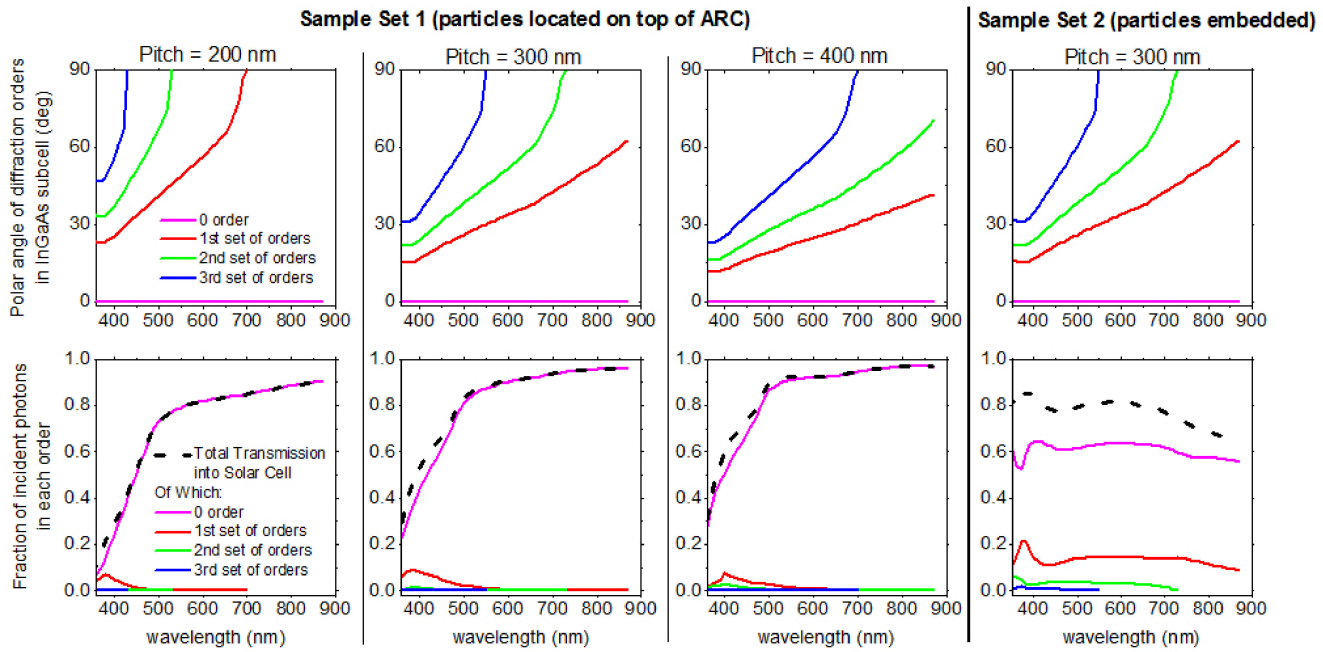


Fig. 4. (Top row) Polar angles of the different sets of propagating diffraction orders within the solar cell that can be coupled to by normally incident light. Graphs are shown for the four NP solar cells fabricated in this study: three from Sample Set 1 and one from Sample Set 2. (Bottom row) Fraction of normally incident photons coupled into each diffraction order (i.e., diffraction efficiencies), as well as the total transmission into the solar cell. Different diffraction orders with the same polar angle are grouped together.

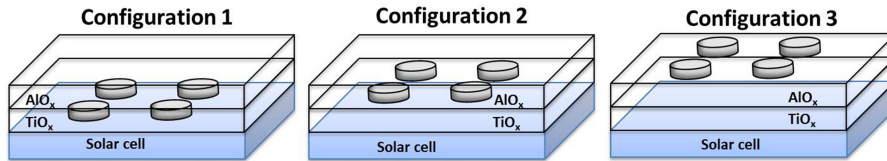


Fig. 5. Schematic of the three configurations for embedding the NPs in the ARC.

cell, this optimization procedure produces a reflectance that is minimal over the 300–900-nm wavelength range and evenly distributed between the individual top- and middle-cell ranges.

A. Solar Cell Structure and Figures of Merit

The assertion that NP arrays can improve MJ solar cells via oblique photon scattering rests on the premise that they can lead to increased absorption in an optically thin subcell. In the wider computational study, this premise is tested directly by choosing the In_{0.01}GaAs middle cell to have a total thickness of 500 nm. This is much thinner than 3.5 μm that would be considered optically thick. All other layer thicknesses are as in the experimental Sample Set 1. To simplify the study, only the performance of the In_{0.01}GaAs middle cell is monitored, since the difficulty of achieving good antireflection in both upper subcells simultaneously has already been investigated by Yang *et al.* [17]. We choose not to use a drift-diffusion model here, but instead make the simplifying assumption that all photogenerated carriers in the middle cell are extracted as current. This is sufficient for the general arguments made in this section. The photocurrent in

each subcell is, therefore, calculated as

$$J_{ph} = q_e \int \Phi(\lambda) A(\lambda) d\lambda \quad (1)$$

where A is the absorption in the In_{0.01}GaAs subcell, and Φ is the incident solar spectrum, which is taken to be AM0.

The NPs are taken to be pure aluminum; for these, we use optical constants from [28]. For all other materials, we use the proprietary optical constants from AzurSpace GmbH.

As an additional study, we also consider the case of Configuration 3 in which the NP material is not aluminum, but rather the same material as the window layer: AlInP. This is motivated by results for black silicon, in which a semiconductor surface is etched directly to reveal semiconductor NPs, producing with remarkably low reflectivities [33].

B. Simulation Results

Due to the large multidimensional parameter space studied, the results are presented as a series of scatterplots, in which every possible (Λ , r , h) combination is represented as a single

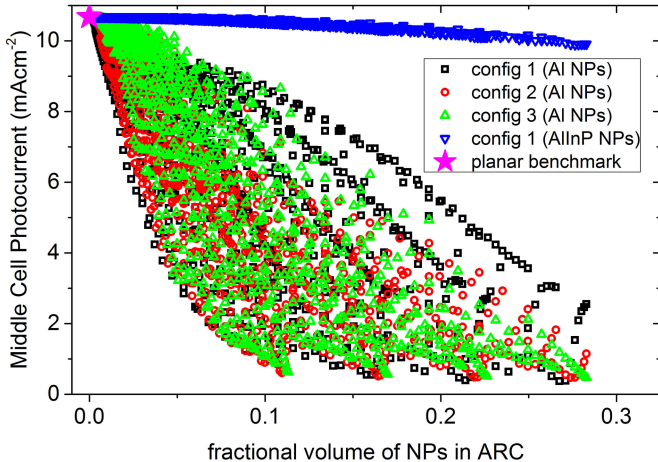


Fig. 6. Scatter plot showing the $\text{In}_{0.01}\text{GaAs}$ middle-cell photocurrent versus the fractional volume of NPs for every combination of dimensions in each configuration. The different configurations correspond to the NPs being embedded in the ARC bottom layer (Configuration 1), embedded in the ARC top layer (Configuration 2) and sitting on top of the ARC (Configuration 3) (see Fig. 5).

marker, where the x - and y -ordinates represent some result of the simulation.

Fig. 6 shows a scatterplot with the calculated photocurrent in the $\text{In}_{0.01}\text{GaAs}$ middle cell as the y -ordinate, and the total volume of NPs as a fraction of the ARC volume (proportional to $h\pi r^2 \Lambda^{-12}$) as the x -ordinate. Note that many combinations of array dimensions can have the same volume fraction, and that the currents shown are much lower than for state-of-the-art cells (even for the benchmark), due to the thin $\text{In}_{0.01}\text{GaAs}$ subcell.

It can be seen that, for all configurations, NP-array dimensions, and materials, the calculated photocurrent is never greater than for the planar benchmark (shown as a magenta star). Introducing metallic NPs anywhere in the ARC generally leads to a decrease in photocurrent if the particles occupy any appreciable volume. In the case of AlInP particles, the photocurrent remains close to the benchmark for all dimensions but never exceeds it. These are the main results of this paper. Although front-side NP arrays have been shown to improve in III-V solar cells in the past [8], [9], these examples were benchmarked against devices with nonoptimal antireflection, as opposed to the optimized double-layer ARC used as comparison here. It has already been shown that Al NPs are unlikely to lead to an improved antireflection compared with an optimized ARC [17]. We add to this by demonstrating clearly the limitations of enhancing the photocurrent of high-efficiency solar cells using Al or AlInP NP arrays on the front face, even in the case where the absorbing layer is extremely thin and requires absorption enhancement via oblique photon scattering. This is explained in the following section in terms of the tradeoff between reduced transmission and improved absorption.

Clearly, a better design must be sought if high-efficiency solar cells are to be improved by front-side nanophotonic light scattering. In the following, we analyze the computational results in order to elucidate some of the problems and form some general design principles to aid this search.

1) Tradeoff Between Oblique Scattering and Transmission: The introduction of NPs (or any other scattering element) onto the front surface can only produce a net improvement if significant oblique scattering can be achieved while maintaining high transmission of incident light into the solar cell. To separate these two factors, we define T to be the transmission of incident light into the solar cell (note that $T = 1 - R - A_{NP}$, where R is the front-surface reflectance, and A_{NP} is the parasitic absorption in the NPs). We also define the quantity internal quantum efficiency (IQE) via

$$\text{EQE}(\lambda) = T(\lambda) \cdot \text{IQE}(\lambda). \quad (2)$$

Since we have assumed full collection of photogenerated charge carriers, the IQE defined in this way represents the probability that a photon, once transmitted into the $\text{In}_{0.01}\text{GaAs}$ subcell, is absorbed there. This depends only on the path length of the photons within the $\text{In}_{0.01}\text{GaAs}$ layer and is thus an ideal measure of the positive contribution made by oblique photon scattering to the overall absorption. This differs from some other definitions of the IQE. Looking at (1) and (2), we can see that we have effectively decomposed the middle-cell photocurrent into transmission-dependent and scattering-dependent components T and IQE, respectively.

We define the integrated spectrum-weighted values of T and IQE as

$$T_\Phi = \frac{\int \Phi(\lambda) T(\lambda) d\lambda}{\int \Phi(\lambda) d\lambda}$$

$$\text{IQE}_\Phi = \frac{\int \Phi(\lambda) \text{IQE}(\lambda) d\lambda}{\int \Phi(\lambda) d\lambda}. \quad (3)$$

The values T_Φ and IQE_Φ have been calculated over the 670–870-nm range, i.e., between the top-cell and middle-cell bandgaps. This is to avoid the analysis being complicated by absorption in the top cell.

For each simulation result, IQE_Φ is plotted against T_Φ in the scatterplot in Fig. 7. This shows clearly the tradeoff between transmission into the solar cell and oblique scattering. Also shown in Fig. 7 is a break-even line. This is a locus of points for which the product $T_\Phi \cdot \text{IQE}_\Phi$ is equal to the same product for the planar benchmark. Any simulation result above this line would yield a net improvement over the planar benchmark.

In the case of metallic NPs, we can see that, for many NP-array dimensions, significant scattering is achieved leading to an increase in IQE_Φ . However, this comes at an even greater loss in transmission into the solar cell, yielding an overall loss. The transmission loss is a combination of increased reflection and parasitic light absorption in the particles themselves. We found on average that the contribution of these two factors to the loss is roughly equal, although for some combinations of NP dimensions, the loss can be dominated by one factor or the other. For the AlInP NPs, transmission remains high, but virtually no scattering is achieved, yielding no improvement.

The difference between Al and AlInP NP behavior may be explained in terms of refractive index contrasts. A high contrast, such as that between a metal and a dielectric, leads to strong scattering but strong reflection (there is also absorption in the

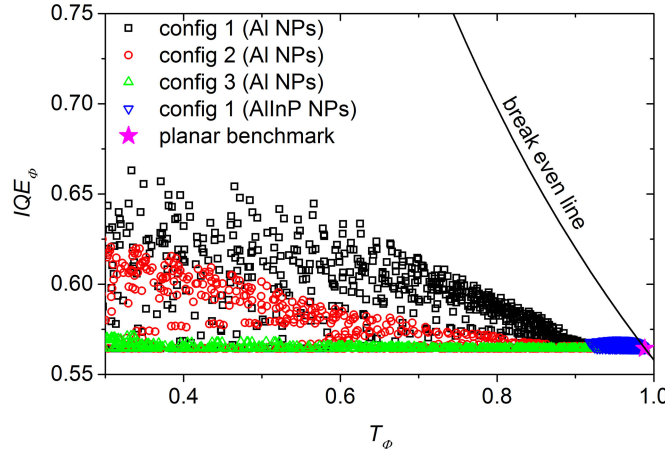


Fig. 7. Scatter plot showing IQE_ϕ versus T_ϕ for every combination of dimensions in each configuration. The different configurations correspond to the NPs being embedded in the ARC bottom layer (Configuration 1), embedded in the ARC top layer (Configuration 2), and sitting on top of the ARC (Configuration 3) (see Fig. 5).

metal, although this can be minimized at solar wavelengths for small Al particles [8]). A low contrast, as between AlInP and TiO_x , maintains good antireflection but achieves little scattering.

2) Requirements for Oblique Scattering: Nanoparticle Position in the Antireflection Coating: From Fig. 7, we see that, for a given T_ϕ , better IQE_ϕ can be achieved by Al particles in configuration 1, followed by configuration 2 and then 3. This suggests that separating the NPs from the semiconductor with a dielectric has the effect of suppressing oblique scattering into the solar cell. To further investigate this, simulations were made in which the gap between the NP base and the semiconductor was varied continuously from 0 to 120 nm. The NP array dimensions were fixed at 270-nm period, 150-nm diameter, and 30 nm height. Fig. 8 shows the coupling efficiency of normally incident light into oblique diffraction orders in the solar cell calculated from these simulations for wavelengths of 700 and 850 nm.

The most striking feature of Fig. 8 is the drop-off of the oblique coupling upon increasing the spacing from a few nanometers toward 120 nm. To explain this, we observe that the critical angle at the interface between the semiconductor ($n \sim 3.5$) and the TiO_x ($n \sim 2$) is around 35° . Therefore, any photon mode that propagates in the semiconductor with a polar angle above 35° must be evanescent in the TiO_x . Similarly, any mode propagating with a polar angle above 25° must be evanescent in the AlO_x ($n \sim 1.5$). Therefore, for a photon interacting with the NPs to couple to a mode in the semiconductor with a significantly large polar angle, it must tunnel through the dielectric spacer, with the coupling efficiency falling off with increasing spacer thickness. We conclude that the spacer should be no greater than a few tens of nanometers if oblique coupling is to be achieved.

Fig. 8 also shows an initial rise of the oblique coupling upon increasing the spacing from 0 to 20 (5) nm for a wavelength of 700 (850) nm. This is in accordance with results in [34]. There, it is shown that a 30-nm spacer layer increases the scattering

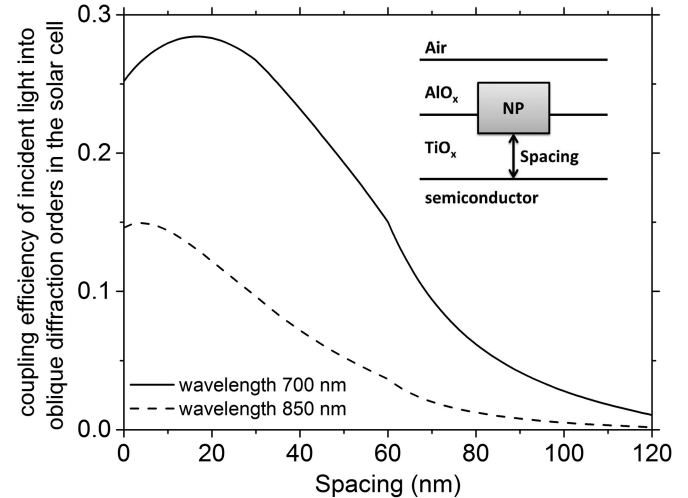


Fig. 8. Coupling efficiency of normally incident light into oblique diffraction orders in the solar cell as a function of the distance between the NP base and the semiconductor. The NP array dimensions are fixed at 270-nm period, 150-nm diameter, and 30 nm height. Results are presented at wavelengths of 700 and 850 nm. At these wavelengths and this array period, only the specular zero-order and the first ring of oblique orders propagate in the semiconductor. The latter propagate at polar angles of 49° and 74° at 700 and 850 nm, respectively. ARC (Configuration 3) (see Fig. 5).

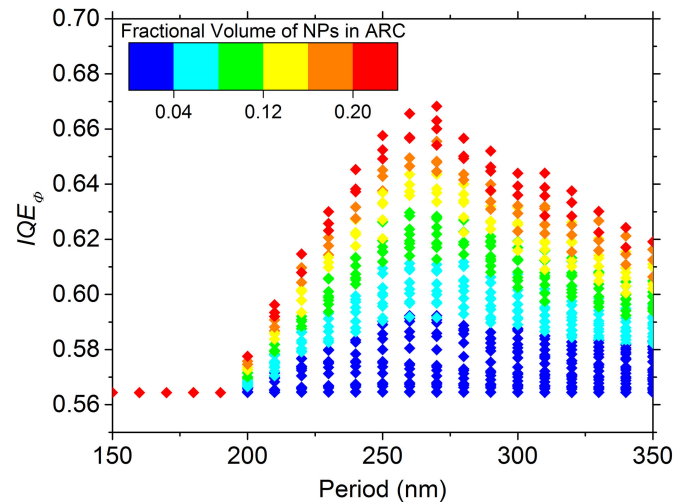


Fig. 9. Scatter plot showing IQE_ϕ versus array period for Al NPs in configuration 1. The color of each symbol represents the fraction volume of NPs for the corresponding combination of dimensions, respectively. ARC (Configuration 3) (see Fig. 5).

cross section of the NPs when compared with a 0-nm spacer layer, due to an increase in the driving field at the location of the NPs. However, in that study, the NPs are not embedded in a dielectric; therefore, a direct comparison is not necessarily valid.

3) Requirements for Oblique Scattering: Array Period and Nanoparticle Volume: To investigate the effect of array period and NP volume on oblique scattering, we focus on the results for Al NPs in configuration 1. For these simulation results, Fig. 9 shows a scatterplot of IQE_ϕ against array period. Note there are many results for each period, due to the range of NP radii and heights studied. The color of each symbol represents the

volume of the NPs as a fraction of the total ARC volume. We observe that there is very little scattering enhancement for low periods, and that the best scattering can be achieved for a period of 270 nm. In addition, for a given period, the enhancement due to scattering increases monotonically with the size of the NPs. These results suggest that the array period and NP volume are of primary importance for aggregate scattering enhancement, whereas the aspect ratio of the NPs is of secondary importance (consider that symbols of a given color represent a range of aspect ratios with similar volumes).

The period dependence of Fig. 9 is explained as follows. Because the NP array is periodic, and the $\text{In}_{0.01}\text{GaAs}$ subcell is in the far field of the array, incident light is coupled into the $\text{In}_{0.01}\text{GaAs}$ subcell via discrete propagating diffraction orders. The onset of the first oblique propagating diffraction orders in the semiconductor is at the wavelength [32]

$$\lambda = n\Lambda \quad (4)$$

where n is the semiconductor refractive index. For higher wavelengths, the only allowed propagating transmitted order is the specular zero order, and there can be no oblique scattering. For array periods below 200 nm, oblique scattering is, therefore, forbidden for the entire $\text{In}_{0.01}\text{GaAs}$ absorption band (see Fig. 4, top left panel 700–900-nm range). At an array period of 270 nm, the onset of the first oblique diffraction order coincides with the $\text{In}_{0.01}\text{GaAs}$ absorption onset at around 900 nm (similar to the top right panel of Fig. 4). At this period, oblique scattering is permitted for the entire $\text{In}_{0.01}\text{GaAs}$ absorption band. Furthermore, the diffraction orders are most oblique close to the $\text{In}_{0.01}\text{GaAs}$ bandgap, meaning that the best absorption enhancement coincides with the range of weak absorption in the $\text{In}_{0.01}\text{GaAs}$. This results can be generalized to say that the best enhancement from oblique scattering can be achieved when $\Lambda = \lambda E_g / n$, where n and λE_g are the refractive index and bandgap wavelength of the target subcell. It is also possible that good enhancement is achieved for larger periods at which higher diffraction orders are introduced. This has not been studied here.

V. DISCUSSION AND OUTLOOK

A. Requirements for Oblique Scattering Versus Requirements for Good Transmission

It is interesting to compare the requirements for oblique scattering presented here with the requirements for good transmission presented in the literature. For metallic NP arrays positioned on the front side of a semiconductor, good transmission requires that the bipolar plasmon resonance is situated close to the ultraviolet onset of the useful solar spectrum [8], [35]. In this work, it has been shown that the requirements for IQE enhancement via oblique scattering are minimizing the dielectric spacing between the NPs and the semiconductor to a few tens of nm (see Section IV-B2), and using relatively large particles (necessitated by the simultaneous need for large period and high fractional volume coverage—Section IV-A3). Both these requirements have the effect of red-shifting the plasmon resonance (see [27] and [36]). This could be partly responsible for the result in Fig. 7 that IQE enhancement via oblique scattering

can only be achieved at the expense of unacceptable losses in transmission into the solar cell.

B. Oblique Scattering Versus Light Trapping

Deflecting incident photons into oblique trajectories in a solar cell can lead to absorption enhancement via two mechanisms. First, the oblique trajectory has a higher path length in a single pass of the solar cell by a factor of $1/\cos\theta$, where θ is the inclination of the photon path. Second, oblique photons can be totally internally reflected at both faces, leading to multiple passes of the absorbing layer, which is often referred to as light trapping [4].

We observe that, in a GaInP/ $\text{In}_{0.01}\text{GaAs}/\text{Ge}$ solar cell, there is no opportunity for this type of light trapping when trying to enhance absorption in the middle cell. Any photon in the $\text{In}_{0.01}\text{GaAs}$ absorption band can make at most one pass of the middle cell, since reflection at the lower $\text{In}_{0.01}\text{GaAs}$ interface is minimal, and the lower bandgap Ge bottom cell is strongly absorbing throughout the $\text{In}_{0.01}\text{GaAs}$ absorption band. This argument also holds when trying to achieve absorption enhancement in the top cell. In the present design, it is, therefore, only possible to achieve absorption enhancement via the obliqueness of paths and not via multiple passes. This argument holds when trying to enhance any of the upper subcells in any MJ solar cell, in which the refractive index contrast between layers is very small, such as those based on bulk III–V compounds and group IV materials.

We can quantify the relative merits of each mechanism using the analysis of Yablonovitch and Cody [37]. This states that, for a semiconductor slab under air, texturing of either or both surfaces and applying a perfect reflector to the rear will lead to an absorption enhancement that tends to $4n^2$ in the limit where the textured surface scatters isotropically. One factor of 2 results from the angular averaging of the photon paths; this is the gain due to the obliqueness of photon paths. The other factor of 2 is due to the perfect reflector; this is not present beneath the target subcell in our MJ cell. The factor of n^2 results from the density of photon states in the material compared with the surrounding air. The n^2 enhancement can only be taken advantage of via multiple passes of the slab due to total internal reflection at both interfaces; this is not possible in our case since the lower subcell has the same index as the target subcell. Since $n^2 \sim 11$ for $\text{In}_{0.01}\text{GaAs}$, Si, etc., we see that multiple passes has far greater importance than mere obliqueness of photon paths. In the present MJ design, we would, therefore, expect absorption enhancements not on the order of $4n^2$ but rather on the order of 2, which is much lower.

Achieving a proper light-trapping effect could be made possible by the inclusion of a wavelength-selective reflector between the middle and bottom cells. This would need to provide omnidirectional reflection in the middle-cell absorption band, but be transmissive in the bottom-cell absorption band. Distributed Bragg reflectors (DBRs) provide such a function for normally propagating light and are compatible with present fabrication methods, having been grown within MJ solar cells in the past [38], [39]. However, for oblique incidence, DBRs exhibit a

blue-shifting of the reflection peak and a significant reduction in the peak reflectance [40]. Hence, they cannot alone provide effective light trapping in the context described in this paper.

A light-trapping design that employs an omnidirectional reflector between the middle and bottom cells and overcomes the problem of transmission loss into the top and middle cells is presented elsewhere [41].

VI. CONCLUSION

Aluminum NP arrays were successfully embedded in the ARC of InGaP/InGaAs/Ge solar cells. In particular, we have demonstrated the integration of these arrays into commercial space solar cells using nanoimprint lithography: a replication technique with potential to realize high throughput and low cost.

Irradiation tests were performed to investigate the effect of NP scattering on current generation in the electrically thinned top and middle junctions. Before irradiation, losses are observed in the EQE due to reduced transmission through the NP-embedded ARC. Losses range from insignificant to extreme, depending on the array dimensions. After irradiation, no improvement is observed in the EQE compared with the control. Computational simulations reveal that oblique photon scattering is weak in these particular NP-embedded-ARC designs, and as such, any gains are eclipsed by the losses.

A fast electrooptical simulation technique has been developed to predict the EQE of MJ solar cells with integrated optical nanostructures. The technique is validated against experiments and then used to study a large parameter space, varying the NP array pitch, height, diameter, and position in the ARC, with nearly 6000 different structures simulated in total. By deconvoluting the photocurrent into transmission and IQE, it is shown that oblique photon scattering does lead to appreciably improved IQE for many designs but that, in all cases, this benefit is outweighed by transmission losses. We conclude that nanophotonic light trapping is possible for the upper junctions in MJ solar cells, but that a radical design change is required to achieve improved performance over the state of the art.

Design principles for strong oblique scattering are established to aid the search for future designs. In particular, we find that for good light trapping, the dielectric spacing between the NPs and the solar cell must be no greater than a few tens of nanometers. What is more, we find that optimal light trapping requires an array period equal to $\lambda Eg/n$, where n and λEg are the refractive index and bandgap wavelength of the target subcell, respectively. Finally, the lower than expected improvement in IQE due to oblique scattering is explained in terms of the lack of an omnidirectional wavelength selective mirror between the target subcell and the cells below.

ACKNOWLEDGMENT

The authors would like to thank O. Höhn, E. Oliva, N. Tucher, and C. Wellens for processing and characterization at Fraunhofer ISE. The solar cells used in this study were provided by AZUR SPACE.

REFERENCES

- [1] L. Zeng *et al.*, "Demonstration of enhanced absorption in thin film Si solar cells with textured photonic crystal back reflector," *Appl. Phys. Lett.*, vol. 93, pp. 221103–221105, 2008.
- [2] S. Mokkapati and K. R. Catchpole, "Nanophotonic light trapping in solar cells," *J. Appl. Phys.*, vol. 112, pp. 101101–101119, 2012.
- [3] V. E. Ferry *et al.*, "Light trapping in ultrathin plasmonic solar cells," *Opt. Exp.*, vol. 18, pp. A237–A245, 2010.
- [4] D. Redfield, "Multiple-pass thin-film silicon solar cell," *Appl. Phys. Lett.*, vol. 25, pp. 647–648, 1974.
- [5] C. Heine and R. H. Morf, "Submicrometer gratings for solar energy applications," *Appl. Opt.*, vol. 34, pp. 2476–2482, 1995.
- [6] J. Zhao, A. Wang, P. Campbell, and M. A. Green, "A 19.8% efficient honeycomb multicrystalline silicon solar cell with improved light trapping," *IEEE Trans. Electron Devices*, vol. 46, no. 10, pp. 1978–1983, Oct. 1999.
- [7] A. Mellor *et al.*, "Nanoimprinted diffraction gratings for crystalline silicon solar cells: Implementation, characterization and simulation," *Opt. Exp.*, vol. 21, pp. A295–A304, 2013.
- [8] N. P. Hylton *et al.*, "Loss mitigation in plasmonic solar cells: Aluminium nanoparticles for broadband photocurrent enhancements in GaAs photodiodes," *Sci. Rep.*, vol. 3, 2013, Art. no. 2874.
- [9] K. Nakayama, K. Tanabe, and H. A. Atwater, "Plasmonic nanoparticle enhanced light absorption in GaAs solar cells," *Appl. Phys. Lett.*, vol. 93, 2008, Art. no. 121904.
- [10] M. Yamaguchi *et al.*, "Super-high-efficiency multi-junction solar cells," *Prog. Photovoltaics, Res. Appl.*, vol. 13, pp. 125–132, 2005.
- [11] T. Takamoto, T. Agui, K. Kamimura, and M. Kaneiwa, "Multijunction solar cell technologies—High efficiency, radiation resistance, and concentrator applications," in *Proc. 3rd World Conf. Photovoltaic Energy Convers.*, 2003, vol. 1, pp. 581–586.
- [12] D. B. Jackrel *et al.*, "Dilute nitride GaInNAs and GaInNAsSb solar cells by molecular beam epitaxy," *J. Appl. Phys.*, vol. 101, pp. 114916–114918, 2007.
- [13] T. Takamoto *et al.*, "World's highest efficiency triple-junction solar cells fabricated by inverted layers transfer process," in *Proc. 35th IEEE Photovoltaic Spec. Conf.*, 2010, pp. 412–417.
- [14] J. F. Geisz, J. M. Olson, M. J. Romero, C. S. Jiang, and A. G. Norman, "Lattice-mismatched GaAsP solar cells grown on silicon by OMVPE," in *Proc. 4th IEEE World Conf. Photovoltaic Energy Conf.*, 2006, pp. 772–775.
- [15] M. R. Lueck *et al.*, "Dual junction GaInP/GaAs solar cells grown on metamorphic SiGe/Si substrates with high open circuit voltage," *IEEE Electron Device Lett.*, vol. 27, no. 3, pp. 142–144, Mar. 2006.
- [16] M. A. Putyato, B. R. Semyagin, E. A. Emel'yanov, N. A. Pakhanov, and V. V. Preobrazhenskii, "Molecular-beam epitaxy of GaAs/Si(001) structures for high-performance tandem A III BV/Si-solar energy converters on an active silicon substrate," *Russian Phys. J.*, vol. 53, pp. 906–913, 2011.
- [17] L. Yang, S. Pillai, and M. A. Green, "Can plasmonic Al nanoparticles improve absorption in triple junction solar cells?" *Sci. Rep.*, vol. 5, Jul. 3, 2015, Art. no. 11852.
- [18] K. R. Catchpole and A. Polman, "Design principles for particle plasmon enhanced solar cells," *Appl. Phys. Lett.*, vol. 93, 2008, Art. no. 191113.
- [19] H. Hauser *et al.*, "Development of nanoimprint processes for photovoltaic applications," *J. Micro/Nanolithography, MEMS, MOEMS*, vol. 14, no. 3, 2015, Art. no. 031210.
- [20] A. J. Wolf *et al.*, "Origination of nano- and microstructures on large areas by interference lithography," *Microelectron. Eng.*, vol. 98, pp. 293–296, Oct. 2012.
- [21] S.-K. Meisenheimer *et al.*, "Large area plasmonic nanoparticle arrays with well-defined size and shape," *Opt. Mater. Exp.*, vol. 4, pp. 944–952, 2014.
- [22] ECSS-E-ST-20-08C Rev.1, ESA, Paris, France, 2012.
- [23] K. Johnson, *Grating Diffraction Calculator (GD-Calc)*, 5th ed. Santa Clara, CA, USA: KJ Innovation, 2005.
- [24] J. Nelson, *The Physics of Solar Cells*. London, U.K.: Imperial Coll. Press, 2003.
- [25] X. Li *et al.*, "Multi-dimensional modeling of solar cells with electromagnetic and carrier transport calculations," *Prog. Photovoltaics, Res. Appl.*, vol. 21, pp. 109–120, 2013.
- [26] X. Li *et al.*, "Bridging electromagnetic and carrier transport calculations for three-dimensional modelling of plasmonic solar cells," *Opt. Exp.*, vol. 19, pp. A888–A896, 2011.

- [27] M. W. Knight *et al.*, "Aluminum for plasmonics," *ACS Nano*, vol. 8, pp. 834–840, 2014.
- [28] E. D. Palik, *Handbook of Optical Constants of Solids*, vols. 1–5, San Diego, CA, USA: Academic, 1997.
- [29] S. A. Maier, *Plasmonics: Fundamentals and Applications*. New York, NY, USA: Springer, 2007.
- [30] M. W. Knight *et al.*, "Aluminum plasmonic nanoantennas," *Nano Lett.*, vol. 12, pp. 6000–6004, 2012.
- [31] P. M. Schwab *et al.*, "Linear and nonlinear optical characterization of aluminum nanoantennas," *Nano Lett.*, vol. 13, pp. 1535–1540, 2013.
- [32] M. Neviere and E. Popov, *Light Propagation in Periodic Media: Differential Theory and Design (Optical Engineering)*. Boca Raton, FL, USA: CRC, 2002.
- [33] P. Spinelli, M. A. Verschueren, and A. Polman, "Broadband omnidirectional antireflection coating based on subwavelength surface Mie resonators," *Nature Commun.*, vol. 3, 2012, Art. no. 692.
- [34] S. Pillai, F. J. Beck, K. R. Catchpole, Z. Ouyang, and M. A. Green, "The effect of dielectric spacer thickness on surface plasmon enhanced solar cells for front and rear side depositions," *J. Appl. Phys.*, vol. 109, 2011, Art. no. 073105.
- [35] P. Spinelli *et al.*, "Optical impedance matching using coupled plasmonic nanoparticle arrays," *Nano Lett.*, vol. 11, pp. 1760–1765, 2011.
- [36] P. Spinelli, C. van Lare, E. Verhagen, and A. Polman, "Controlling Fano lineshapes in plasmon-mediated light coupling into a substrate," *Opt. Exp.*, vol. 19, pp. A303–A311, May 2011.
- [37] E. Yablonovitch and G. D. Cody, "Intensity enhancement in textured optical sheets for solar cells," *IEEE Trans. Electron Devices*, vol. ED-29, no. 2, pp. 300–305, Feb. 1982.
- [38] D. B. Bushnell *et al.*, "Short-circuit current enhancement in Bragg stack multi-quantum-well solar cells for multi-junction space cell applications," *Sol. Energy Mater. Sol. Cells*, vol. 75, pp. 299–305, 2003.
- [39] D. C. Johnson *et al.*, "Observation of photon recycling in strain-balanced quantum well solar cells," *Appl. Phys. Lett.*, vol. 90, 2007, Art. no. 213505.
- [40] D. Bushnell, "Optimisation of strain-compensated multi-quantum well solar cells," Ph.D. dissertation, Dept. Phys., Imperial Coll. London, London, U.K., 2003.
- [41] A. Mellor, N. P. Hylton, S. A. Maier, and N. Ekins-Daukes, "Interstitial light-trapping design for multi-junction solar cells," *Sol. Energy Mater. Sol. Cells*, 2016, under review.

Authors' photographs and biographies not available at the time of publication.